IEEE Access
Multidisciplinary | Rapid Review | Open Access Journal

Received January 14, 2021, accepted January 21, 2021, date of publication January 26, 2021, date of current version January 29, 2021.

Digital Object Identifier 10.1109/ACCESS.2021.3054618

A Coaxial Alignment Method for Large Flange Parts Assembly Using Multiple Local Images

WEICHEN SUN, ZHIJING ZHANG, AND WEIMIN ZHANG
School of Mechanical Engineering, Beijing Institute of Technology, Beijing 100081, China

Corresponding author: Zhijing Zhang (zhzhj@bit.edu.cn)

This work was supported by the Joint Fund of Advanced Aerospace Manufacturing Technology Research under Project U1937603 and Project U1737207.

ABSTRACT The large flange parts in aero-engines are usually manually assembled. Collision damage caused by assembly alignment error often occurs in the assembly process, which affects the assembly accuracy and product reliability. The machine vision-based alignment methods usually achieve the high-precision measurement of the parts by obtaining the high-resolution images of the whole parts with a combination of laser distance sensors. Hence, existing methods are high costly and inefficient. In this paper, a new alignment method based on the principle of coaxial alignment for large flange parts is proposed. The proposed method first obtains multiple high-precision image pairs from the local field of views at the fitting surfaces of flanges. The clearance and bolt holes in each image pair are then extracted via edge recognition and Hough Transformation. Two optimization models are built to calculate the translation adjustment and rotation adjustment. The optimization model 1 is built with the translation adjustments of the flange as the variables and the consistency of the clearances as the objective function. The algorithm to solve the model based on the gradient-descent method is proposed. The positions of the bolt holes in the images are subsequently adjusted based on the translation adjustment, and the rotation adjustment is calculated by solving the built optimization model 2. The experiments show that the proposed method can be applied to the assembly process of large flange parts, and the visual servo control model based on this method also has good stability.

INDEX TERMS Coaxial alignment, large flange parts, assembly, machine vision.

I. INTRODUCTION

During the assembly processes of aero-engines, many large rotary parts need to be aligned. At present, the assembly processes of these parts are usually achieved manually with the assistance of spreaders. Flanges, with large cylindrical structure and the fitting relationship of hole and shaft, are commonly used slewing parts of aero-engines. As manual assembly cannot accurately adjust the relative translation and direction errors between the flanges, a large assembly alignment error often occurs in the assembly process, causing collision damage which affects the assembly accuracy and product reliability. Hence, developing the online inspection and automatic alignment methods for large flange assembly could reduce manual labor intensity and increase the assembly success rate.

The recognition and measurement methods of industrial parts based on machine-vision have been greatly developed and widely applied [1]. Several sorts of commercial software have also been applied in the manufacturing and assembly processes of mechanical parts [2]. The machine-vision based assembly systems generally utilize the pattern matching methods, which find the matching features of the known image and target image, to locate, feed, and assemble the parts [3]. These matching methods include geometric based methods [4], [5] and feature-descriptors based methods [6], [7]. The geometric based methods generally extract geometric features of the parts (such as points, straight lines, and arcs) and then match the features with known geometric models to achieve positioning of parts. Doignon *et al.* achieved the positioning of parts by extracting feature points and estimating the transformation matrix between the feature points [8]. Liu *et al.* used Hough transform to stably recognize and locate the circular parts [9]. Cha *et al.* used the ellipse feature(extracted by the Hough transform) and the linear support vector machine to classify the loosened bolts [10]. Arjun *et al.* recognized and assembled the parts by matching the template shape and the geometric features

The associate editor coordinating the review of this manuscript and approving it for publication was Guangcun Shan.

of the parts [11]. Rusli *et al.* recognized and assembled automotive fasteners via a template matching method [12]. The feature-descriptors-based methods achieve parts recognition and positioning via extracting and matching the feature descriptors in the part images and template images. Bohlool *et al.* recognized the parts by background segmentation and matching of the SIFT features [13]. Doerr *et al.* used ORB features to recognize and classify various industrial parts [14]. Zheng *et al.* used ORB features to locate and grab mechanical parts [15]. As long as been localized, the parts can be adjusted and assembled by driving the motion modules, such as motion platforms or robots, in the assembly systems. Such systems have been applied to achieve assembly processes of parts. Liu *et al.* accomplished the assembly of small parts by utilizing three cameras to detect the posture of the parts and a force sensor to detect the assembly force [16]. Ye *et al.* designed a coaxial alignment assembly system and analyzed the error of the system to achieve the alignment and assembly of small parts with accuracy better than 5um [17], [18].

The specially designed jigs and fixtures with high manufacturing accuracy are generally used to grab the part for the assembly of large parts, hence the position of the part is ensured. As the large parts are difficult to be precisely measured by simply using the whole image of the part, various measuring instruments, such as coordinate-measuring machines and laser distance sensors (LDS), are combined to measure and localize the large parts. Due to the circular shapes, the measurement of flanges is generally achieved by recognizing and localizing the key geometric features of the flanges, such as centers of circles. Huang *et al.* used the laser displacement sensors to detect the profile lines and achieve the measurement of flanges in trains [19]. Wang *et al.* proposed a fast measurement method for flange-end holes using multi-camera to locate the flange-end holes with a position accuracy of 0.1mm [20]. The position of deep-sea pipeline is also obtained with high accuracy by localizing the center of flange [21]. Airbus uses the Measurement-Assisted Assembly method (MAA) based on laser trackers to assemble the fuselage and wing components of the aircraft, reducing the cost of jigs and fixtures and increasing efficiency [22]. Liu *et al.* used a CCD camera and an LDS in the AGV system to recognize and localize the part by detecting the point and circle features of the parts, and then accomplished the assembly of large components [23]. Li *et al.* improved Liu's method by acquiring images via coaxially distributed cameras and fitting the edges as ellipses, and then aligned the components by building and solving an optimization model via Particle Swarm Optimization (PSO) method [24]. Some other kinds of large parts, such as radar antennas and large frames were also assembled by using cameras, LDS, and inclination angle sensors [25]–[27].

However, all the above methods perform part recognition and localization by acquiring the image of the entire part. The accuracy of measurement for the part is affected by the resolution of the image. Using a high-resolution camera with the combination of a wide-angle lens could improve the measurement accuracy, but will also increase the hardware costs. The measurement error caused by the distortion of the wide-angle lens also makes the high-accuracy measurement of large parts difficult to achieve with a single camera. In some cases, only a part of the image features of the flanges (usually the circular contours) can be acquired due to the occlusion of other structures. Although the contours of the flanges are known to be circular, estimating the positions of the flanges using a small part of the features will lead to a large positioning error. Using other sensors such as LDS could improve the measurement accuracy, but there often be an error between the measurement position and the part benchmark, which will lead to inaccurate localization result. Overall, the above methods could not achieve a balance between cost and measurement accuracy.

This paper presents a novel coaxial alignment method for large flange parts, as shown in Fig. 1. The method first obtains multiple high-precision image pairs from the local field of views (FOVs) at the fitting surfaces of flanges. The edge and bolt holes are extracted via edge recognition and Hough Transformation, and the value and direction of clearance in each image pair are subsequently analyzed and calculated. The corresponding relationship between the adjustment of the flange and clearance is analyzed. The optimization model 1 is then built with the translation adjustment as the variable and the consistency of the clearances as the objective function. The translation adjustment is then obtained by solving the optimization model 1 using the proposed gradient-descent-based algorithm. The positions of the bolt holes in the images are subsequently adjusted using the translation adjustment, and optimization model 2 is built with the rotation adjustment of the flange as the variable and the center distance of bolt holes as the objective function. The optimization model 2 is subsequently solved via the modified Gaussian barebones differential evolution (MGBDE) algorithm [28]. The proposed method does not require image stitching to obtain all the features of the part, nor a high position accuracy of the camera during image acquisition, reducing the hardware cost of the assembly system. The Experiments show that the proposed method has good alignment accuracy to meet the requirement of assembly of large flanges.

II. DESIGN OF THE ASSEMBLY SYSTEM FOR LARGE FLANGE PARTS BASED ON THE COAXIAL ALIGNMENT METHOD

A. THE PRINCIPLE OF COAXIAL ALIGNMENT

The principle of high-precision alignment based on coaxial alignment is shown in Fig. 2. The target part and base part are fixed by the jigs and moved to the inspection position. By setting a cubic prism with a total reflection film and a splitting film between the target part and base part, the camera could acquire images of the base part and target part in the same image coordinate system (ICS). The relative posture error can be calculated by comparing the postures of the target part and base part in the ICS. The posture of the target part

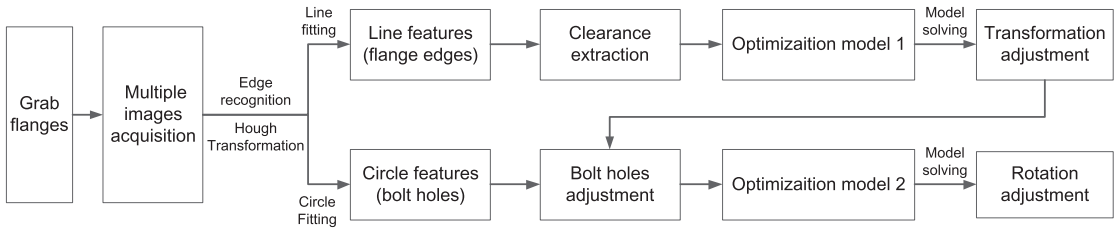

FIGURE 1. The flow chart of the proposed method.

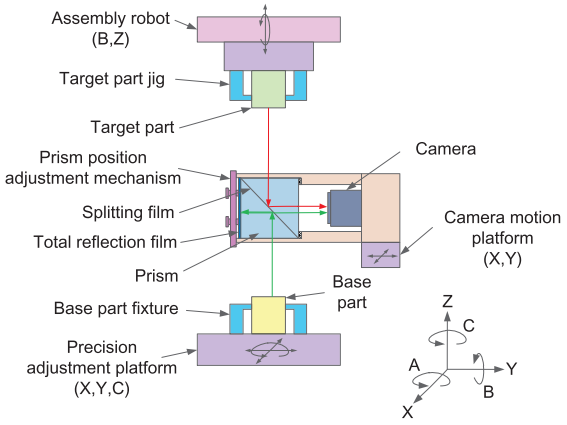

FIGURE 2. The principle of coaxial alignment (The letters below each motion module indicate its motion degree of freedom (DOF)).

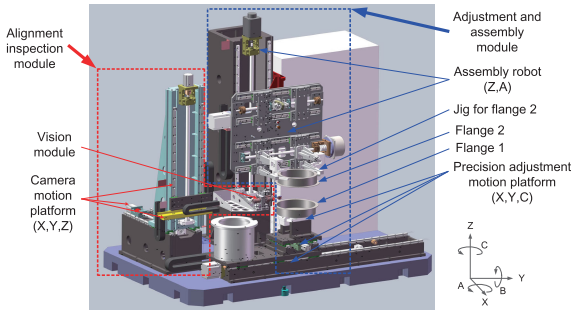

FIGURE 3. The structure design of alignment and assembly system.

can be adjusted via the precision adjustment platform, and the target part can be assembled by moving the assembly robot down along the Z-axis.

B. THE STRUCTURE DESIGN OF ALIGNMENT AND ASSEMBLY SYSTEM FOR LARGE FLANGE PARTS

Based on the coaxial alignment principle, the structure of the alignment and assembly system for large flanges is designed as shown in Fig. 3. In this paper, we define that in a pair of flanges to be assembled, the flange with the larger diameter is flange 1 and the other is flange 2.

The alignment and assembly system is mainly composed of the adjustment and assembly module, and the alignment inspection module. The adjustment and assembly module is composed of the assembly robot, jigs, and the precision adjustment motion platform. The assembly robot has the motion DOFs of vertical movement along the Z-axis and rotation around the X-axis to achieve the loading, unloading, and turning for the flanges. The precision adjustment motion platform has the motion DOFs of horizontal movement along the X- and Y-axis, and the rotation around the Z-axis, providing the function of precise adjustment for flanges.

The alignment inspection module is mainly composed of the vision module and camera motion platform. The vision module mainly includes the camera, lens, and prism to achieve the image acquisition of flanges. The camera motion platform has the motion DOFs of movement along the X, Y, and Z axes, which can achieve the acquisition of multiple images for flanges by loading the vision module at different positions. The alignment and assembly system has been built as shown in Fig. 4.

III. THE COAXIAL ALIGNMENT METHOD BASED ON MULTIPLE LOCAL IMAGES

The posture error between flange 1 and flange 2 includes the translation error and direction error. The translation error makes the clearances between the edges of the two flanges differ greatly at different positions, and the direction error makes the bolt holes of the two flanges to be misaligned. These errors need to be adjusted through the translation adjustment and rotation adjustment respectively to achieve the assembly of the flanges.

In this paper, the multiple images are firstly acquired from the local FOVs at the fitting surface of flanges, forming the image pairs. The two images in each image pair are acquired in the same local FOV, respectively corresponding to the image of flange 1 and flange 2. The edge points in the image pairs are extracted, and the circles and lines are then recognized via Hough transformation and Random Sample Consensus(RANSAC) method to localize the edges and bolt holes of flanges. A two-step method is then employed to calculate the translation adjustment and rotation adjustment of the flanges. First, the clearances between the edges of flange 1 and flange 2 are calculated via the extracted lines. The optimization model 1 is built and the translation adjustment is calculated. Subsequently, the positions of the bolt holes are corrected via the calculated translation adjustment, and the

(a)

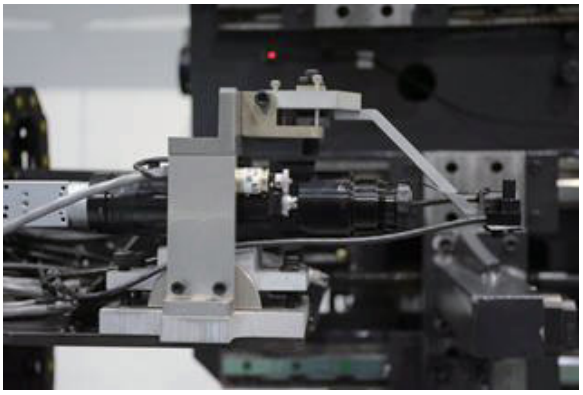

(b)

FIGURE 4. The alignment and assembly system: (a) the assembly system; (b) the vision module.

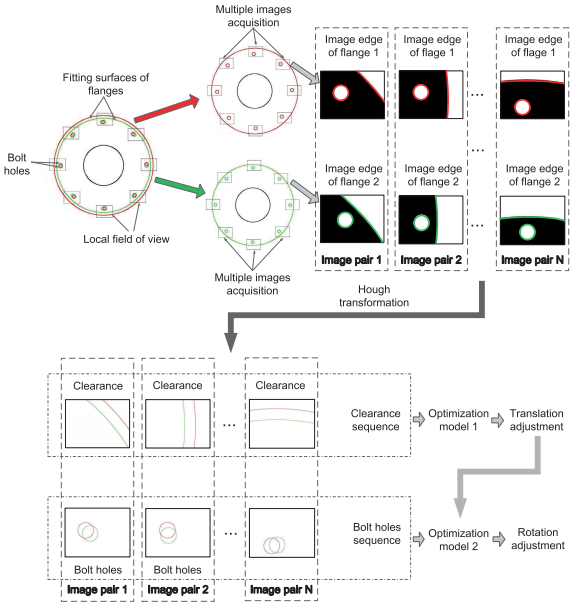

FIGURE 5. The multiple images acquisition, extraction of clearances and bolt holes.

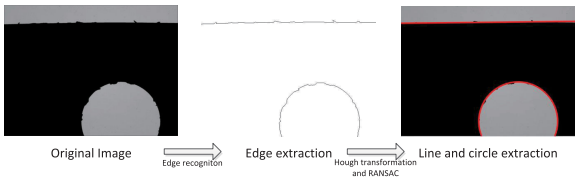

FIGURE 6. The extraction of lines and circles.

rotation adjustment is calculated by building and solving the optimization model 2. The flow chart of the proposed method is shown in Fig. 5.

A. EXTRACTION OF LINES AND CIRCLES IN MULTIPLE IMAGES FROM LOCAL FOVs

By acquiring images at different positions using the vision module, multiple image pairs of the two flanges at the fitting surface are obtained. Each image pair includes the edges and bolt holes of flange 1 and flange 2. These images are pre-processed to remove noise, and the edge points are extracted by utilizing the edge recognition operator (such as Canny). In each image of the local FOV, the flange edge is line-like and the bolt hole is circle-like.

The positions of the extracted edge points are extracted and the circles in the images are recognized via the Hough transformation. By calculating the distance between the edge points and center of the circle, the edge points near the circle are extracted and the other edge points are used to estimate the parameters of the lines. However, there are often many outliers in the edge points owing to the dust and burrs. To reduce the influence of the outliers on model fitting, the RANSAC and Least Squares methods are utilized to estimate the parameters of the circles and lines. The flange edges and bolt holes in the images are respectively extracted, as shown in Fig. 6.

B. MODELING AND CALCULATION OF TRANSLATION ADJUSTMENT

As the diameters of flange 1 and flange 2 are different, the straight lines in each image pair do not coincide, forming the clearance. The clearances in the image pairs are also different due to the translation error. As long as flange 1 and flange 2 are aligned,, the sizes of clearances should be close to the same.

1) CALCULATION OF CLEARANCE DIRECTION

In the image pair acquired from the i-th local FOV, the extracted line points of flange 1 and flange 2 are obtained as point sets $\left\{P_{1l}^{ki}\left(x_{l1}^{(ki)}, y_{l1}^{(ki)}\right)\right\}$ and $\left\{P_{2l}^{ki}\left(x_{l2}^{(ki)}, y_{l2}^{(ki)}\right)\right\}$, (x, y) is the image coordinate of each point. These points are centralized to the same image coordinate system to form the clearance, as shown in Fig. 7.

The line fittings are implemented via the principal component analysis (PCA) and singular value decomposition (SVD) based method. Assuming the equations of line 1($L_1^{(i)}$, edge of flange 1) and line 2 ($L_2^{(i)}$, edge of flange 2) are:

$$\begin{cases} L_1^{(i)} : A_1^{(i)}x + B_1^{(i)}y + C_1^{(i)} = 0, & Flange\ 1 \\ L_2^{(i)} : A_2^{(i)}x + B_2^{(i)}y + C_2^{(i)} = 0, & Flange\ 2 \end{cases} \quad (1)$$

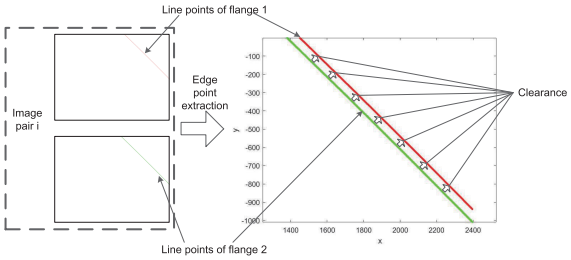

FIGURE 7. The centralization of lines in the i-th image pair and clearance formation.

The optimization model for line 1 fitting is built as:

$$\mathbf{n} = \arg\min_{\|\mathbf{n}\|=1} \mathbf{n}^T \mathbf{P} \mathbf{n} \tag{2}$$

where

$$\mathbf{P} = \begin{bmatrix} \sum \left(x_{l1}{}^{(ki)}\right)^2 & \sum x_{l1}{}^{(ki)} y_{l1}{}^{(ki)} & \sum x_{l1}{}^{(ki)} \\ \sum x_{l1}{}^{(ki)} y_{l1}{}^{(ki)} & \sum \left(x_{l1}{}^{(ki)}\right)^2 & \sum y_{l1}{}^{(ki)} \\ \sum x_{l1}{}^{(ki)} & \sum y_{l1}{}^{(ki)} & 1 \end{bmatrix},$$

$$\mathbf{n} = \begin{pmatrix} A_1{}^{(i)} \\ B_1{}^{(i)} \\ C_1{}^{(i)} \end{pmatrix}.$$

The direction of $\mathbf{n}$ is equal to the eigenvector corresponding to the smallest eigenvalue of $\mathbf{P}$. Line 2 ($L_2^{(i)}$) can be fitted via the same method. Hence the equations of line 1 and line 2 can be obtained.

As shown in Fig. 8, the clearance direction vector $\mathbf{v}_{cd}{}^{(i)}$ in the i-th image pair is defined as the direction from $L_2^{(i)}$ to $L_1^{(i)}$. The clearance direction base vector $\mathbf{v}_{cdb}{}^{(i)}$ is calculated by the parameters of fitted line equations.

$$\mathbf{v}_{cdb}{}^{(i)} = \left(\frac{A_1{}^{(i)} + A_2{}^{(i)}}{2}, \frac{B_1{}^{(i)} + B_2{}^{(i)}}{2} \right)^T \tag{3}$$

The intercept vectors of line 1 $\mathbf{v}_{cinter1}$ and line 2 $\mathbf{v}_{cinter2}$ are calculated via the four intersection points of line 1 and line 2 on the x- and y- axes of image coordinate system. The directions of $\mathbf{v}_{\text{cinter1}}{}^{(i)}$ and $\mathbf{v}_{\text{cinter2}}{}^{(i)}$ are ensured to be from $L_2^{(i)}$ to $L_1^{(i)}$.

$$\mathbf{v}_{\text{cinter1}}{}^{(i)} = \left(0, -\frac{C_1{}^{(i)}}{B_1{}^{(i)}} + \frac{C_2{}^{(i)}}{B_2{}^{(i)}} \right)^T \tag{4}$$

$$\mathbf{v}_{cinter2}{}^{(i)} = \left(-\frac{C_1{}^{(i)}}{A_1{}^{(i)}} + \frac{C_2{}^{(i)}}{A_2{}^{(i)}}, 0 \right)^T \tag{5}$$

The clearance direction vector $\mathbf{v}_{cd}{}^{(i)}$ is defined as the projection vector of $\mathbf{v}_{\text{cinter1}}{}^{(i)}$ (or $\mathbf{v}_{\text{cinter2}}{}^{(i)}$) on $\mathbf{v}_{cdb}{}^{(i)}$, and normalized as $\mathbf{v}^{*(i)}_{cd}$.

$$\mathbf{v}_{cd}{}^{(i)} = \frac{(\mathbf{v}_{\text{cinter}}{}^{(i)})^T \mathbf{v}_{cdb}{}^{(i)}}{(\mathbf{v}_{cdb}{}^{(i)})^T \mathbf{v}_{cdb}{}^{(i)}} \mathbf{v}_{cdb}{}^{(i)} \tag{6}$$

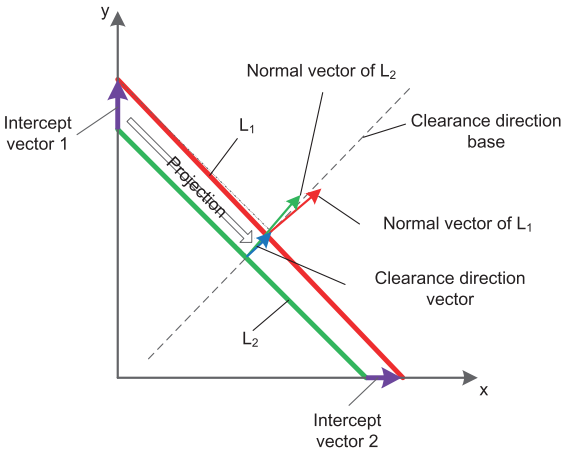

FIGURE 8. The calculation of clearance direction vector.

$$\mathbf{v}^{*(i)}_{cd} = \frac{\mathbf{v}_{cd}{}^{(i)}}{\|\mathbf{v}_{cd}{}^{(i)}\|} \tag{7}$$

2) CLEARANCE VECTOR GENERATION

$L_1^{(i)}$ and $L_2^{(i)}$ are not parallel lines due to the discrete distribution of the edge points and noise, therefore the clearance size cannot be calculated by the line equations. In this paper, the distances between each point of $L_1^{(i)}$ and $L_2^{(i)}$ in the i-th image pair are first calculated. These distances are then sorted in ascending order, and the average value of the first 50% is taken as the clearance size $Cd^{(i)}$. The clearance vector $\mathbf{c}^{(i)}$ is generated via $Cd^{(i)}$ and normalized clearance direction vector $\mathbf{v}^{*(i)}_{cd}$.

$$\mathbf{c}^{(i)} = Cd^{(i)} \mathbf{v}^{*(i)}_{cd} \tag{8}$$

3) EFFECT OF TRANSLATION ADJUSTMENT ON CLEARANCE VECTOR

During the alignment process, the position of flange 1 will be adjusted by driving the precision adjustment motion platform with translation adjustment of $\Delta\mathbf{t} = (\Delta x, \Delta y)^T$, where Δx and Δy express the coordinates of the translation adjustment in the image coordinate system. The clearance will change due to the translation adjustment, as shown in Fig. 9. The clearance change is the projection vector of $\Delta\mathbf{t}$ on $\mathbf{v}^{*(i)}_{cd}$ and the new clearance vector $\mathbf{c}_n{}^{(i)}$ will be:

$$\mathbf{c}_n{}^{(i)} = \frac{(\mathbf{c}^{(i)})^T (\mathbf{c}^{(i)} - \Delta\mathbf{t})}{(\mathbf{c}^{(i)})^T \mathbf{c}^{(i)}} \mathbf{c}^{(i)} = \frac{(\mathbf{c}^{(i)})^T (\mathbf{c}^{(i)} - \Delta\mathbf{t})}{\sqrt{(\mathbf{c}^{(i)})^T \mathbf{c}^{(i)}}} \mathbf{v}^{*(i)}_{cd} \tag{9}$$

The FOV direction vector $\mathbf{v}_{FOVd}{}^{(i)}$ is defined as the direction from the center of flange 1 to the i-th local FOV in the image coordinate system, as shown in Fig. 10. When the flange 1 and flange 2 are aligned, the angle between $\mathbf{v}^{*(i)}_{cd}$ and $\mathbf{v}_{FOVd}{}^{(i)}$ in each image pair should be an acute angle. The clearance symbol $Csig^{(i)}$ is defined as:

$$Csig^{(i)} = \text{Sgn}\left((\mathbf{v}^*{}_{cd}{}^{(i)})^T \mathbf{v}_{FOVd}{}^{(i)} \right) \tag{10}$$

where $\text{Sgn}(\cdot)$ is the sign function.

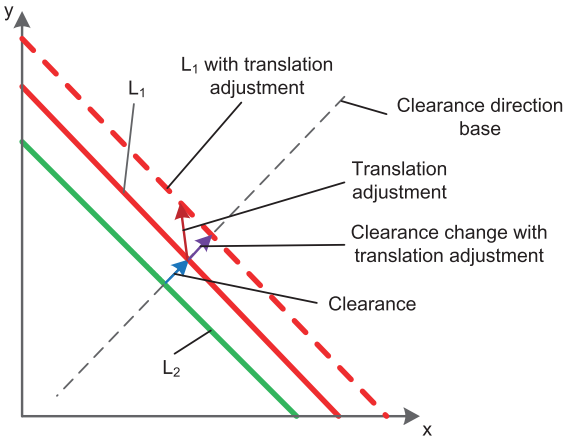

FIGURE 9. Effect of translation adjustment on clearance vector.

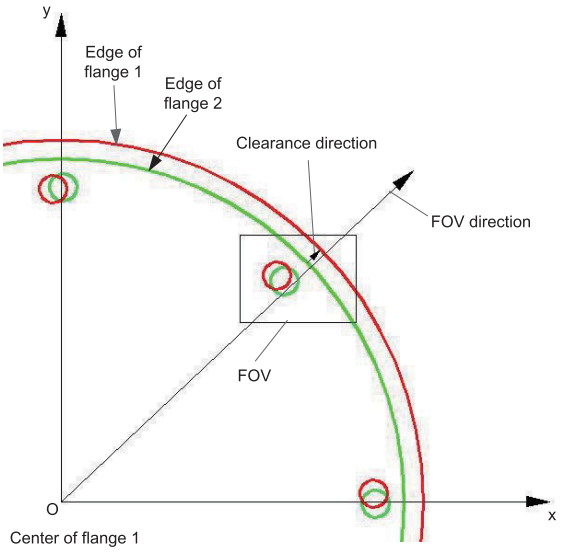

FIGURE 10. The clearance direction and FOV direction should be roughly the same when flange 1 and flange 2 are aligned.

When the direction of $\mathbf{v}^*{}_{cd}{}^{(i)}$ and $\mathbf{v}_{FOVd}{}^{(i)}$ is nearly the same, $Csig^{(i)}$ is $+1$, indicating that clearance direction meets the requirement of alignment, otherwise $Csig^{(i)}$ is -1. The new clearance size $Cn^{(i)}$ with translation adjustment $\Delta\mathbf{t}$ is generated via $Csig^{(i)}$ and $\mathbf{c}_n{}^{(i)}$.

$$Cn^{(i)} = Csig^{(i)} \left\| \mathbf{c}_n{}^{(i)} \right\| = Csig^{(i)} \frac{(\mathbf{c}^{(i)})^T (\mathbf{c}^{(i)} - \Delta\mathbf{t})}{\sqrt{(\mathbf{c}^{(i)})^T \mathbf{c}^{(i)}}} \quad (11)$$

4) THE OPTIMIZATION MODEL 1 FOR TRANSLATION ADJUSTMENT CALCULATION

As long as the flange 1 and flange 2 are aligned, the signs and values of the clearances $\{Cn^{(i)}\}$ should be the same. Therefore, the consistency of $\{Cn^{(i)}\}$ can be used to evaluate the translation error of flange 1 and flange 2. The clearance sequence $\mathbf{Cns}\{Cn^{(1)}, Cn^{(2)}, \ldots, Cn^{(N)}\}$ is generated via $Cn^{(i)}$ in all local FOVs and the variance of clearance sequence var(**Cns**) is used to measure the consistency of the clearance sequence. var(**Cns**) is a function of $\Delta\mathbf{t}$.

$$\begin{aligned} \text{var}(\mathbf{Cns}) &= \frac{1}{N} \sum_{i=1}^{N} (Cn^{(i)} - \text{avg}(\mathbf{Cns}))^2 \\ &= \frac{1}{N} \sum_{i=1}^{N} (Csig^{(i)} \frac{(\mathbf{c}^{(i)})^T (\mathbf{c}^{(i)} - \Delta\mathbf{t})}{\sqrt{(\mathbf{c}^{(i)})^T \mathbf{c}^{(i)}}} - \text{avg}(\mathbf{Cns}))^2 \end{aligned} \quad (12)$$

where N is the number of local FOVs, avg(**Cns**) is the average value of **Cns**.

The flange 1 and flange 2 are aligned when var(**Cns**) is minimum. The objective function of optimization model 1 $L_t(\Delta\mathbf{t})$ is built as:

$$L_t(\Delta\mathbf{t}) = \sum_{i=1}^{N} (C\ sig^{(i)} \frac{(\mathbf{c}^{(i)})^T (\mathbf{c}^{(i)} - \Delta\mathbf{t})}{\sqrt{(\mathbf{c}^{(i)})^T \mathbf{c}^{(i)}}} - \text{avg}(\mathbf{Cns}))^2 \quad (13)$$

The optimization model 1 is built as:

$$\min_{\Delta\mathbf{t}} \sum_{i=1}^{N} (C\ sig^{(i)} \frac{(\mathbf{c}^{(i)})^T (\mathbf{c}^{(i)} - \Delta\mathbf{t})}{\sqrt{(\mathbf{c}^{(i)})^T \mathbf{c}^{(i)}}} - \text{avg}(\mathbf{Cns}))^2 \quad (14)$$

5) THE SOLVING ALGORITHM OF OPTIMIZATION MODEL 1

We present an algorithm based on gradient-decent to solve the optimization model 1. As the partial derivative of avg(**Cns**) to $\Delta\mathbf{t}$ is complicated and avg(**Cns**) changes little after one iteration step, we use the clearance average value of $(k-1)$-th iteration step $\text{avg}(\mathbf{Cns})_{k-1}$ to calculate the gradient direction of $L_t(\Delta\mathbf{t})$ instead of $\text{avg}(\mathbf{Cns})_k$. The gradient direction of $L_t(\Delta\mathbf{t})$ in k-th iteration step is:

$$\begin{aligned} \frac{\partial L_t}{\partial \Delta\mathbf{t}_k} = 2 \sum_{i=1}^{N} \left(Csig^{(i)} \frac{(\mathbf{c}^{(i)})^T (\mathbf{c}^{(i)} - \Delta\mathbf{t}_k)}{\sqrt{(\mathbf{c}^{(i)})^T \mathbf{c}^{(i)}}} - \text{avg}(\mathbf{Cns})_{k-1} \right) \\ * Csig^{(i)} \frac{(\mathbf{c}^{(i)})}{\sqrt{(\mathbf{c}^{(i)})^T \mathbf{c}^{(i)}}} \end{aligned} \quad (15)$$

Setting the searching step-length as α, the iterative formula of $\Delta\mathbf{t}$ is:

$$\Delta\mathbf{t}_{k+1} = \Delta\mathbf{t}_k - \alpha \frac{\partial L_t}{\partial \Delta\mathbf{t}_k} \quad (16)$$

By setting the maximum number of iterations and termination conditions, the optimization model 1 can be solved to obtain the optimal solution $\Delta\mathbf{t}_{opt} = (\Delta x_{opt}, \Delta y_{opt})^T$, which is the translation adjustment.

C. MODELING AND CALCULATION OF ROTATION ADJUSTMENT

The center distance between the bolt hole of flange 1 and flange 2 in each image pair exists due to the translation error and direction error, see Fig. 11. The bolt hole center of flange 1 $(x_{c1}^{(i)}, y_{c1}^{(i)})$ in each image pair is corrected to be

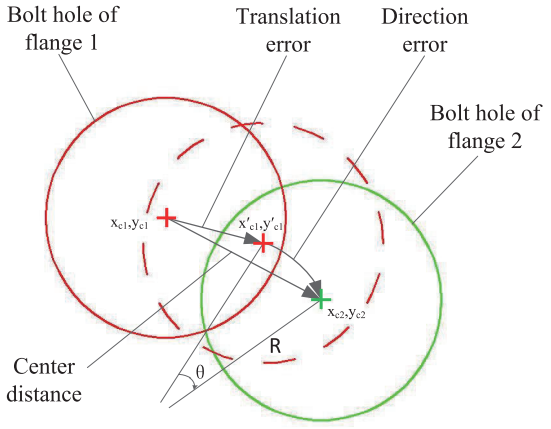

FIGURE 11. The diagram of the visual servo control model.

$(x_{c1}^{(i)'}, y_{c1}^{(i)'})$ via the calculated translation adjustment $\Delta\mathbf{t}_{opt} = (\Delta x_{opt}, \Delta y_{opt})$, and the center distance between the corrected bolt hole of flange 1 $(x_{c1}^{(i)'}, y_{c1}^{(i)'})$ and bolt hole of flange 2 $(x_{c2}^{(i)}, y_{c2}^{(i)})$ is only caused by the direction error. The center distance is evaluated by the rotation angle θ and the distribution radius of the bolt holes $R^{(i)}$. Hence, the optimization model 2 for rotation adjustment calculation is built with θ and $R^{(i)}$ as the variables, and the sum of center distances from all image pairs as the objective function, see (17).

$$\min_{\theta, R^{(i)}} \sum_{i} \left\| \left(x_{c2}^{(i)}, y_{c2}^{(i)}\right) - \left(x_{c1}^{(i)}, y_{c1}^{(i)}\right) - \Delta\mathbf{t}_{opt} \right\| - R^{(i)}\theta \quad (17)$$

In the optimization model 2, θ is a small angle adjustment. Although the value of $R^{(i)}$ is unknown due to the manufacturing errors, the value range can be obtained via the design tolerance of flanges. The model can be solved using the optimization algorithm to obtain the rotation adjustment θ_{opt}.

D. THE VISUAL SERVO CONTROL MODEL OF THE ASSEMBLY SYSTEM

During the adjusting process of the parts, the image of the parts can be acquired using the camera and the adjustment can be updated iteratively. A better alignment effect can be obtained using the proposed coaxial alignment method through multiple iterations. Therefore, a visual servo control model can be designed based on the proposed method. The visual servo control model extracts the incremental motion of the flange feature in image, and performs feedback control on the assembly platforms to achieve the alignment control of the flanges.

1) THE TRANSLATION OF INCREMENTAL MOTION FROM IMAGE COORDINATE SYSTEM TO PHYSICAL CARTESIAN SPACE

In the visual servo control model, the features are extracted in the image coordinate system using the acquired images while

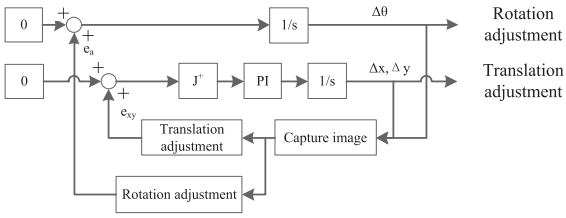

FIGURE 12. The diagram of the visual servo control model.

the adjustments are implemented in the physical Cartesian space using the adjustment platforms. Therefore, the translation of incremental motion from the image coordinate system to the physical Cartesian space is needed to realize the feedback of the control model. The image Jacobian matrix is often used as the translation matrix from the image to physical Cartesian space in the visual servo control models. In this paper, the camera is sensitive to the motions of the adjustment platform in X-, Y-direction and rotation around Z-direction. The relationship of the incremental motions from image to physical Cartesian space is given in (18) and (19).

$$\begin{bmatrix} \Delta u \\ \Delta v \end{bmatrix} = \begin{bmatrix} J_{11} & J_{12} \\ J_{21} & J_{22} \end{bmatrix} \begin{bmatrix} \Delta x \\ \Delta y \end{bmatrix} = \mathbf{J} \begin{bmatrix} \Delta x \\ \Delta y \end{bmatrix} \quad (18)$$

$$\Delta\theta_i = \Delta\theta_p \quad (19)$$

where $(\Delta u, \Delta v, \Delta\theta_i)$ are the increments of features in the image coordinate system and $(\Delta x, \Delta y, \Delta\theta_p)$ are the increments of adjustment platform motions in the physical Cartesian space. $\mathbf{J}$ is the Jacobian matrix.

2) THE DESIGN OF VISUAL SERVO CONTROL MODEL

Based on the analysis in III-D1, the visual servo control model is designed as shown in Fig. 12. The model consists of the translation adjustment control model and the rotation adjustment control model. The images of each FOV is captured, and the translation adjustment and rotation adjustment are calculated through the method proposed in III-B and III-C. The calculated adjustments are transformed to the physical Cartesian space using the Jacobian matrix and are fed back to form the closed loop control. Different from other existing visual servo control methods, the target of the proposed control model is not a position of one part but the relative pose error of the two flanges to be assembled. The translation and rotation error should be 0 after the proper adjustment. Therefore, the target value of translation adjustment and rotation adjustment are 0s. The PI controller is applied to the translation adjustment control model and the control law is given in (20). The control system is stable when the PI controller is well adjusted.

$$\begin{bmatrix} \Delta x \\ \Delta y \end{bmatrix} = K_p \mathbf{J}^{-1} \left(\begin{bmatrix} \Delta u_k \\ \Delta v_k \end{bmatrix} - \begin{bmatrix} \Delta u_{k-1} \\ \Delta v_{k-1} \end{bmatrix} \right) + K_i \mathbf{J}^{-1} \begin{bmatrix} \Delta u_k \\ \Delta v_k \end{bmatrix} \quad (20)$$

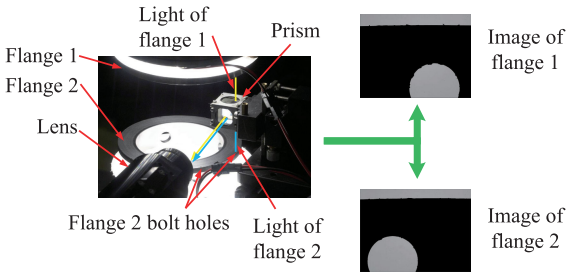

FIGURE 13. The acquisition of image pairs from local FOVs.

TABLE 1. The clearance size $Cd^{(i)}$ [pixel], clearance vector $\mathbf{c}^{(i)}$ [pixel, pixel], direction of FOV $\mathbf{v}_{FOVd}{}^{(i)}$ and clearance symbol $Csig^{(i)}$ of each image pair.

i	$Cd^{(i)}$[pixel]	$\mathbf{c}^{(i)}$[pixel,pixel]	$\mathbf{v}_{FOVd}{}^{(i)}$	$Csig^{(i)}$
1	40.12	$(0.32, -40.12)^T$	$(0, -1)^T$	1
2	48.09	$(-33.86, -34.14)^T$	$(-1, -1)^T$	1
3	28.02	$(-20.81, -0.25)^T$	$(-1, 0)^T$	1
4	8.07	$(-5.79, 5.62)^T$	$(-1, 1)^T$	1
5	40.61	$(0.37, -40.61)^T$	$(0, 1)^T$	-1
6	47.21	$(-33.26, -33.51)^T$	$(1, 1)^T$	-1
7	27.39	$(-27.39, -0.23)^T$	$(1, 0)^T$	-1
8	7, 23	$(5.19, -5.03)^T$	$(1, -1)^T$	1

where the symbol $\mathbf{J}^{-1}$ represents the inverse of image Jacobian matrix $\mathbf{J}$. K_p and K_i are the proportional and integral factors of the PI controller, k is the sampling moment.

IV. EXPERIMENT

The proposed method was tested on a smaller prototype to verify its effectiveness. The diameters of flange 1 and flange 2 are 100.05mm and 100mm. Eight bolt holes with a diameter of 1mm and a distribution diameter of 97.5 $\pm$ 0.1mm were evenly distributed on each flange, forming the bolt hole pairs. The flange 1 and flange 2 were first aligned, and then the flange 1 is translated and rotated, forming the translation error and a direction error of 1° between the flange 1 and flange 2.

As shown in Fig. 12, the image pairs were acquired from the eight local FOVs which contain the meeting surface and the bolt hole pairs. By using the lens with a magnification of 4x, the pixel equivalent of each image was calibrated to be 0.918um/pixel. The acquired image pairs were shown in Fig. 14.

A. THE CALCULATION OF TRANSLATION AND ROTATION ADJUSTMENT

Using the method proposed in III, the clearance (clearance size $Cd^{(i)}$ and clearance vector $\mathbf{c}^{(i)}$ in each image pair were extracted, and the clearance symbol of each local FOV was calculated using the known position of each local FOV in the world coordinate system, as shown in Table 1.

The translation adjustment was calculated using the proposed method in III-B. The optimization model 1 was built and solved using the proposed algorithm in III-B5. By setting the initial iteration translation adjustment $\Delta\mathbf{t}_0 = (0, 0)^T$,

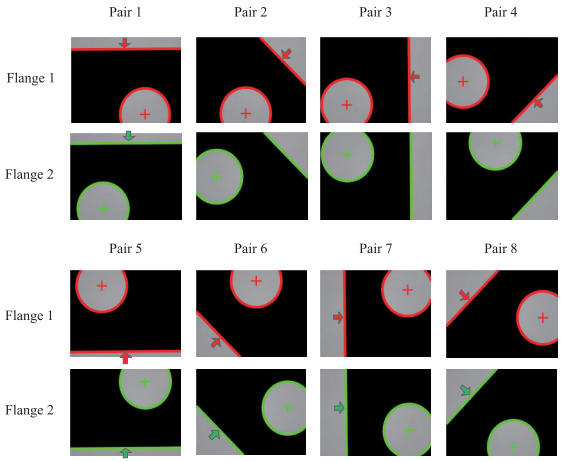

FIGURE 14. The acquired image pairs and the extracted geometric features: the arrows and crosses indicate the extracted edge lines and bolt hole centers.

TABLE 2. The optimization results of different initial iteration translation adjustment and error.

$\Delta\mathbf{t}_0$ $[pixel, pixel]$	Δx_{opt} $[pixel]$	Δy_{opt} $[pixel]$	Δx_{opt} $[um]$	Δy_{opt} $[pixel]$
$(8, 8)^T$	-30.39	-37.21	-111.43	-27.90
$(-13, 9)^T$	-30.40	-37.16	-111.48	-27.91
$(-44, 7)^T$	-30.46	-37.17	-111.71	-27.96
$(-68, -13)^T$	-30.51	-37.21	-111.90	-28.01
$(-63, -47)^T$	-30.55	-37.30	-112.03	-28.04
$(-52, -71)^T$	-30.48	-37.34	-111.77	-27.98
$(-23, -73)^T$	-30.42	-37.35	-111.55	-27.93
$(-3, -67)^T$	-30.38	-37.34	-111.40	-27.89
$(12, -47)^T$	-30.35	-37.29	-111.29	-27.86
$(15, -16)^T$	-30.34	-37.22	-111.26	-27.85

the search steplength $\alpha = 0.05$, the maximum iteration number maxiter $= 100$, the termination condition $\varepsilon = 0.05$, the solution of the optimization model 1 was obtained as $\Delta\mathbf{t}_{opt} = (-30.34, -37.15)^T$, the correspond translation adjustment in the world coordinate system was $\Delta x_{opt} = -27.85$um, $\Delta y_{opt} = -34.10$um.

The stability of the proposed method was tested by setting different initial values of iterations. The optimization results with different initial values were shown in Table 2. For the different initial iteration translation adjustment, the proposed algorithm could converge to the vicinity of the optimal solution. By calculating the value of objective function $L_t(\Delta\mathbf{t})$ near the optimal solution, the shape of $L_t(\Delta\mathbf{t})$ was found to be similar to a convex function, as shown in Fig. 15. Therefore, the proposed solving algorithm for translation adjustment based on the gradient descent method was proved to be fast and stable.

The bolt hole positions of flange 1 and flange 2 in each image pair were extracted and then be corrected using the calculated translation adjustment $\Delta\mathbf{t}_{opt} = (-30.34, -37.15)^T$, as shown in Table 3.

The optimization model 2 to calculate the rotation adjustment was built using the method proposed in III-C. In this

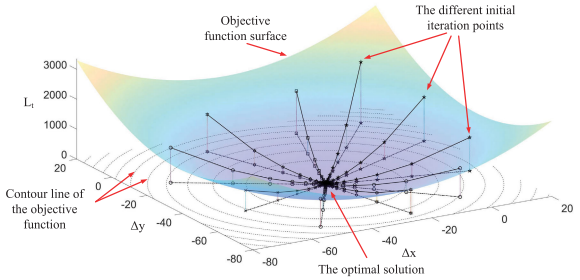

FIGURE 15. The proposed algorithm stably converges to the optimal solution.

TABLE 3. The bole hole positions of flange 1 and flange 2.

Image pair No.	Bolt hole positions of flange 1 $(x_{c1}^{(i)}, y_{c1}^{(i)})$ [pixel,pixel]	Bolt hole positions of flange 2 $(x_{c2}^{(i)}, y_{c2}^{(i)})$ [pixel,pixel]
1	$(704.96, -1566.60)^T$	$(1609.57, -1599.34)^T$
2	$(435.37, -910.18)^T$	$(1079.20, -1600.49)^T$
3	$(586.63, -453.38)^T$	$(572.52, -1417.93)^T$
4	$(1050.14, -210.64)^T$	$(360.73, -926.65)^T$
5	$(1625.58, -272.32)^T$	$(680.80, -321.05)^T$
6	$(1998.33, -826.27)^T$	$(1295.82, -218.97)^T$
7	$(1919.51, -1278.55)^T$	$(1888.81, -404.08)^T$
8	$(1453.19, -1610.31)^T$	$(2069.24, -972.54)^T$

paper, the MGBDE algorithm was used to solve the optimization model 2 and obtain the rotation adjustment. The paprameters of the MGBDE algorithm were set to: population is 15, the maximum number of iterations is 15. The optimization result was 1.0037°, which differs from the actual angle error of 1° by 0.0037°.

B. THE ASSEMBLY OF THE FLANGES USING CALCULATED ADJUSTMENTS

After the translation and rotation adjustments are obtained, the flanges could be assembled. However, the motions of translation and rotation adjusting are coupled in many assembly systems. In assembly system designed in this paper, the coupling is mainly caused by the misalignment of rotation centers between of the part and rotating adjustment platform. As shown in Fig. 16, the rotation adjustment will affect the position of the part, but the translation adjustment will not change the direction of the part. The translation caused by the rotation adjustment is given in (21)

$$\Delta l = R_e \Delta\theta \tag{21}$$

where Δl represents the translation; R_e represents the eccentric distance from the part center to the rotation center of adjustment platform; $\Delta\theta$ represents the rotation adjustment.

According to (21), the coupling of translation and rotation adjustments are effect by the eccentric distance and the direction error between the flanges. There are two methods to solve this problem: (1) By reasonably designing the fixture(self-centering fixture such as three-jaw chuck) and standardizing the clamping position of the flanges(pre-positioning the flanges), R_e and $\Delta\theta$ will be very

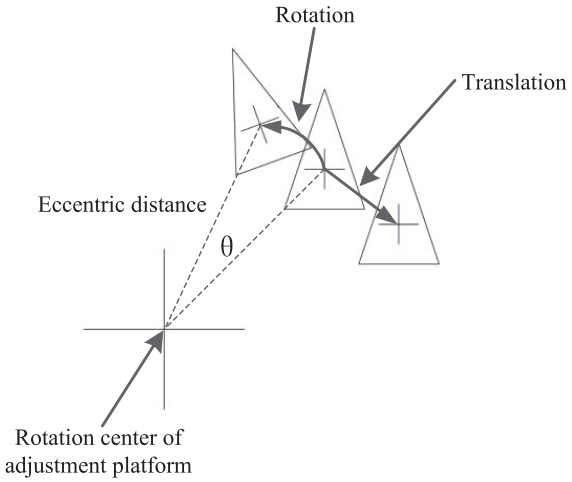

FIGURE 16. The misalignment of rotation centers between of the part and rotating adjustment platform causes the coupling of rotation adjustment and translation adjustment.

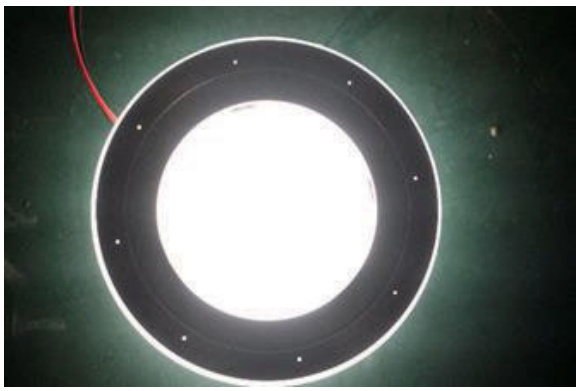

FIGURE 17. The aligned and assembled flanges.

small($R_e < 0.05mm$ and $\Delta\theta < 5°$). The translation caused by the rotation adjustment is less than $5um$, which has little effect on the assembly of the flanges; (2) In more general cases, R_e and $\Delta\theta$ are unknown and the value of Δl could not be estimated. The direction error of the flange is first adjusted using the calculated rotation adjustment and the direction error is eliminated. The translation adjustment is recalculated and performed subsequently. Both of the two methods can be iterated multiple times to achieve better assembly results.

The flanges were aligned and successfully assembled with the calculated adjustments, which shows that the accuracy of the proposed alignment method is better than the one-side design clearance of flange 1 and flange 2 by 25um, as shown in Fig. 17.

C. THE VISUAL SERVO CONTROL OF THE ASSEMBLY SYSTEM

1) THE STABLITY OF THE VISUAL SERVO CONTROL MODEL

The visual servo control model was simulated on the assembly system using the Simmechanics module in Matlab, as shown in Fig. 18. According to the pixel equivalent of the

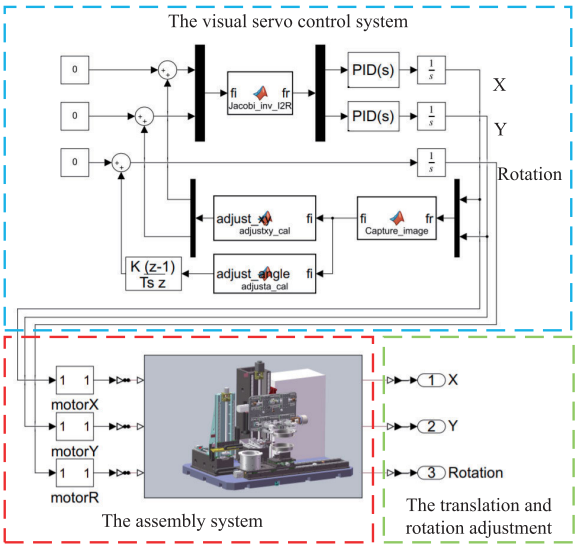

FIGURE 18. The simulation model built using Simmechanics.

TABLE 4. The pre-designed enable signal of sequence controller.

Step	1	2	3	4	5	6	7	8	9	10
g_1	*		*		*		*		*	
g_2		*		*		*		*		*

vision system, the Jacobian matrix of the visual servo control model was set as:

$$\mathbf{J} = \begin{bmatrix} 1089.32 & 0 \\ 0 & 1089.32 \end{bmatrix} \tag{22}$$

The adjustments output by the control model after each iteration step was applied to the edge points extracted in the images of flange 1 shown in Fig. 14, and the new clearances of the image pairs were re-calculated to obtain the new adjustment, which were fed back to form the visual servo control system. The adjustment results of the assembly system are shown in Fig. 19. The translation adjustments in X direction and Y direction converge to −33.6um and −40.2um. The rotation adjustment converges to 1.0046°. The proposed visual servo control model is proved to have good and stability.

2) THE APPLYMENT OF THE VISUAL SERVO CONTROL MODEL

The visual servo control model was then applied to the assembly system. The flowchart of the visual servo control strategy is shown in Fig. 20. A sequence controller was employed to achieve the separately control of the rotation adjustment and translation adjustment(see IV-B). The sequence controller sends a pre-designed enable signal to the gate controller g_1 and g_2 in each adjustment step, making the rotation adjustment and translation adjustment performed step by step. The pre-designed enable signal is shown in Table 3('*' means enable).

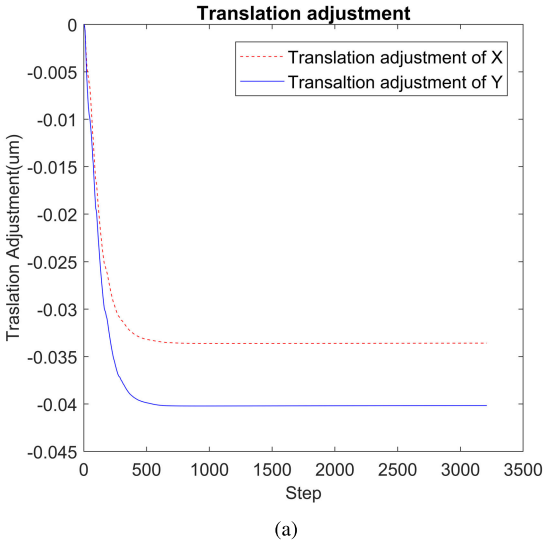

FIGURE 19. The translation adjustment and rotation adjustment: (a) translation adjustment; (b) rotation adjustment.

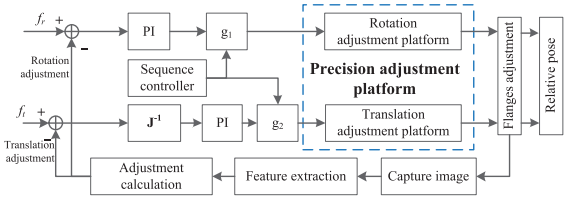

FIGURE 20. The flowchart of the visual servo control strategy.

The Jacobian matrix was calibrated by acquiring the image of a calibration bord which moving along the X- and Y-direction of the precision adjustment platform. The calibrated Jacobian matrix is:

$$\mathbf{J} = \begin{bmatrix} 1088.7 & 47.6 \\ -38.1 & 1088.3 \end{bmatrix} \tag{23}$$

The errors during the alignment process are given in Fig. 21. Due to the sequence control(see Table 4), the

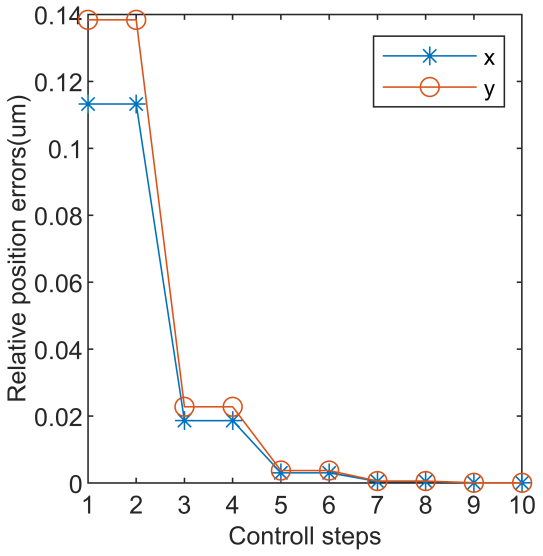

FIGURE 21. The errors in the alignment process: (a) translation errors; (b) direction error.

translation errors and direction error were adjusted every other step. The alignment process was performed stably and smoothly.

V. CONCLUSION

In this paper, a novel coaxial alignment method for large flange parts is proposed. The structure of the alignment and assembly system is designed and built. The proposed method extracts the clearances and bolt holes in the image pairs acquired in several local FOVs instead of acquiring the whole images of flanges. The relationship between the clearance and the translation adjustment is analyzed and the optimization model 1 to calculate the translation adjustment is built with the consistency of the clearance sequence as the objective function and the translation adjustment as the variables. The solving algorithm for optimization model 1 based on the gradient descent method is proposed. Therefore, the positions of the bolt holes can be corrected using the calculated translation adjustment. The optimization model 2 to calculate the rotation adjustment is then built with the sum of center distances of corrected bolt holes as the objective function and the rotation adjustment and the distribution radius as the variables. The optimization model 2 is then solved using MGBDE algorithm. The visual servo control model could be built and achieve a stable adjustment after multiple iterations using the proposed method. The proposed method is proved to be stable through the experiment and can be applied to achieve the large flange assembly.

Despite the successful application of the proposed method in the assembly process of large flange parts, some limitations remain and further improvements are essential. The clearance in each local FOV is extracted using the fitted equations of lines, which are recognized using Hough transform. For some general mechanical parts with complex shapes, the edges appear as complex curves in the local FOVs. In this case, using the Hough transform would cause failure and the clearance extraction method need to be improved. The recognition of keypoint-features in local FOVs may be applied to calculate the clearances of the general mechanical parts. In future work, the optimization model 1 and optimization model 2 will be modified to calculate the adjustments for general mechanical parts and various assembly types.

REFERENCES

[1] D. Braggins and C. Connolly, "Machine vision advances and applications," *Assem. Autom.*, vol. 29, no. 2, pp. 106–111, 2009.
[2] D. Braggins, "Vision today for assembly automation," *Assem. Autom.*, vol. 26, no. 3, pp. 181–183, Jul. 2006.
[3] A. A. Malik, M. V. Andersen, and A. Bilberg, "Advances in machine vision for flexible feeding of assembly parts," *Procedia Manuf.*, vol. 38, pp. 1228–1235, Jan. 2019.
[4] K. Kanatani and Y. Sugaya, "Performance evaluation of iterative geometric fitting algorithms," *Comput. Statist. Data Anal.*, vol. 52, no. 2, pp. 1208–1222, Oct. 2007.
[5] T. T. Pham, T.-J. Chin, K. Schindler, and D. Suter, "Interacting geometric priors for robust multimodel fitting," *IEEE Trans. Image Process.*, vol. 23, no. 10, pp. 4601–4610, Oct. 2014.
[6] D. G. Lowe, "Distinctive image features from scale-invariant keypoints," *Int. J. Comput. Vis.*, vol. 60, no. 2, pp. 91–110, Nov. 2004.
[7] Y. Zhang and Z. Miao, "Object recognition based on ORB and self-adaptive kernel clustering algorithm," in *Proc. ICSP*, Hangzhou, China, 2014, pp. 1397–1402.
[8] C. Doignon, G. Abba, and E. Ostertag, "Recognition and localization of solid objects by a monocular vision system for robotic tasks," in *Proc. IROS*, Munich, Germany, 1994, pp. 2007–2014.
[9] Y. Liu, J. Zhang, and J. Tian, "An image localization system based on gradient Hough transform," *Proc. SPIE*, vol. 9815, Dec. 2015, Art. no. 98151F.
[10] Y.-J. Cha, K. You, and W. Choi, "Vision-based detection of loosened bolts using the Hough transform and support vector machines," *Autom. Construct.*, vol. 71, pp. 181–188, Nov. 2016.
[11] P. Arjun and T. T. Mirnalinee, "Machine parts recognition and defect detection in automated assembly systems using computer vision techniques," *Revista Técnica de la Facultad de Ingeniería Universidad del Zulia*, vol. 39, no. 1, pp. 71–80, 2016.
[12] L. Rusli and A. Luscher, "Fastener identification and assembly verification via machine vision," *Assem. Autom.*, vol. 38, no. 1, pp. 1–9, Feb. 2018.

[13] M. Bohlool and S. R. Taghanaki, "Cost-efficient automated visual inspection system for small manufacturing industries based on SIFT," in *Proc. IVCNZ*, Christchurch, New Zealand, 2008, pp. 1–6.
[14] K. Doerr, J. Samarabandu, and X. Wang, "Efficient object classification using multiple views in manufacturing environments," in *Proc. ICIAfS*, Colombo, Sri Lanka, 2014, pp. 1–5.
[15] Z. Zheng, Y. Ma, H. Zheng, Y. Gu, and M. Lin, "Industrial part localization and grasping using a robotic arm guided by 2D monocular vision," *Ind. Robot, Int. J.*, vol. 45, no. 6, pp. 794–804, Oct. 2018.
[16] S. Liu, D. Xu, D. Zhang, and Z. Zhang, "High precision automatic assembly based on microscopic vision and force information," *IEEE Trans. Autom. Sci. Eng.*, vol. 13, no. 1, pp. 382–393, Jan. 2016.
[17] X. Ye, J. Gao, Z. Zhang, C. Shao, and G. Shao, "An improved vision calibration method for coaxial alignment microassembly," *Assem. Autom.*, vol. 34, no. 3, pp. 237–243, Jul. 2014.
[18] X. Ye, P. Liu, Z. Zhang, C. Shao, and Y. Li, "Error sensitivity analysis of a microassembly system with coaxial alignment function," *Assem. Autom.*, vol. 36, no. 1, pp. 25–33, Feb. 2016.
[19] W. Huang, X. Cheng, Z. Xing, Y. Zhang, and Y. Qin, "A method of flange size measurement based on laser displacement sensor," in *Proc. EITRT*, Berlin, Germany, 2016, pp. 299–307.
[20] L. Wang, G. Lu, and Y. Sun, "The fast measurement for the relative position of flange-end holes," *IEEE Access*, vol. 7, pp. 29149–29157, 2019.
[21] Z. Wang, H.-X. Dang, T. Wang, and B. Zhang, "Development of a position measuring device of a deep-sea pipeline based on flange center positioning," *J. Mar. Sci. Eng.*, vol. 8, no. 2, p. 86, Feb. 2020.
[22] B. Marguet and B. Ribere, "Measurement-assisted assembly applications on airbus final assembly lines," *SAE Trans.*, vol. 112, no. 1, pp. 372–375, 2003.
[23] H. Liu, W. Zhu, and Y. Ke, "Pose alignment of aircraft structures with distance sensors and CCD cameras," *Rob. Comput. Integr. Manuf.*, vol. 48, pp. 20–38, Dec. 2017.
[24] S. Li, Z. Deng, Q. Zeng, and X. Huang, "A coaxial alignment method for large aircraft component assembly using distributed monocular vision," *Assem. Autom.*, vol. 38, no. 4, pp. 437–449, Sep. 2018.
[25] G. Peng, Y. Sun, R. Han, C. Li, and S. Liu, "A measuring method for large antenna assembly using laser and vision guiding technology," *Measurement*, vol. 92, pp. 400–412, Oct. 2016.
[26] Z. Qin, P. Wang, J. Sun, and H. Qiao, "Polygon detection and localization based on link-line model," in *Proc. WCICA*, Shenyang, China, 2015, pp. 1874–1880.
[27] Z. Qin, P. Wang, J. Sun, J. Lu, and H. Qiao, "Precise robotic assembly for large-scale objects based on automatic guidance and alignment," *IEEE Trans. Instrum. Meas.*, vol. 65, no. 6, pp. 1398–1411, Jun. 2016.
[28] M. F. Yeh, H. C. Lu, T. H. Chen, and M. S. Leu, "Modified Gaussian barebones differential evolution with hybrid crossover strategy," in *Proc. ICMLC*, Jeju, South Korea, 2017, pp. 7–12.

WEICHEN SUN received the B.S. degree from Beijing Jiaotong University, Beijing, China, in 2011. He is currently pursuing the Ph.D. degree with the Beijing Institute of Technology. His research interests include machine vision, intelligent manufacturing, and image processing.

ZHIJING ZHANG is currently a Professor with the School of Mechanical Engineering, Beijing Institute of Technology. His current research interests include precision micro machine manufacturing, intelligent manufacturing, and precision microstructure simulation technology.

WEIMIN ZHANG received the M.S. degree from the Dalian University of Technology, China, in 1988, and the Ph.D. degree from the National Technical University of Ukraine, Ukraine, in 1994. He is currently a Professor with the School of Mechanical Engineering, Beijing Institute of Technology. His current research interests include mechanical testing technology, sensor design and production, and electromagnetic nondestructive testing technology.